A new EC–PC threshold estimation method for neural spike detection

2012 J. Neural Eng. 9 046017

(http://iopscience.iop.org/1741-2552/9/4/046017)

J. Neural Eng. **9** (2012) 046017 (16pp) doi:10.1088/1741-2560/9/4/046017

A new EC–PC threshold estimation method for *in vivo* neural spike detection

Zhi Yang[1,5], Wentai Liu[2], Mohammad Reza Keshtkaran[1], Yin Zhou[1], Jian Xu[1], Victor Pikov[3], Cuntai Guan[4] and Yong Lian[1]

[1] Department of Electrical and Computer Engineering, National University of Singapore, Singapore 119077, Singapore
[2] Department of Bioengineering and California Nanosystems Institute, UCLA, Los Angeles, CA 900095-1600, USA
[3] Huntington Medical Research Institutes, Pasadena, CA 91105, USA
[4] Institute for Infocomm Research, Agency for Science, Technology and Research, Singapore 138632, Singapore

E-mail: eleyangz@nus.edu.sg

Received 14 December 2011
Accepted for publication 8 June 2012
Published 13 July 2012
Online at stacks.iop.org/JNE/9/046017

Abstract
This paper models *in vivo* neural signals and noise for extracellular spike detection. Although the recorded data approximately follow Gaussian distribution, they clearly deviate from white Gaussian noise due to neuronal synchronization and sparse distribution of spike energy. Our study predicts the coexistence of two components embedded in neural data dynamics, one in the exponential form (noise) and the other in the power form (neural spikes). The prediction of the two components has been confirmed in experiments of *in vivo* sequences recorded from the hippocampus, cortex surface, and spinal cord; both acute and long-term recordings; and sleep and awake states. These two components are further used as references for threshold estimation. Different from the conventional wisdom of setting a threshold at 3×RMS, the estimated threshold exhibits a significant variation. When our algorithm was tested on synthesized sequences with a different signal to noise ratio and on/off firing dynamics, inferred threshold statistics track the benchmarks well. We envision that this work may be applied to a wide range of experiments as a front-end data analysis tool.

(Some figures may appear in colour only in the online journal)

1. Introduction

Understanding a neural code responsible for information representation, generation and transmission is one of the important problems in neuroscience toward demystifying the neuronal substrate of intelligence, cognitive function and memory [1–4]. Intensive neurophysiological experiments [5–7], neuroprothetic studies [8, 9] and computational modeling effort [10, 11] have been reported to infer a potential neural code, and code candidates include 'firing-rate', 'synchrony propagation', or a combination of the two [8, 12–15]. For all the candidates, they take spiking activities from neural ensembles as input. In this sense, reliably detecting spikes from neurophysiological recordings is a prerequisite for information decoding. In general, the detected spike rate is very sensitive to detection threshold, implying a great deal of uncertainty in harvested information regardless of the choice of neural code [16]. After a few decades of electrophysiology experiments and algorithm development [11, 17–20, 20–29], experimentalists and theoreticians still raise the question in various occasions: how do you set the detection threshold? A trade-off is that if one lowers the detection threshold too much, a large portion of threshold crossing activities become attributed to noise; raising the threshold, on the other hand, gets rid of these false detections at a cost of nonlinearly reducing information content. This is further complicated by several imposed constraints. For example,

[5] Author to whom any correspondence should be addressed.

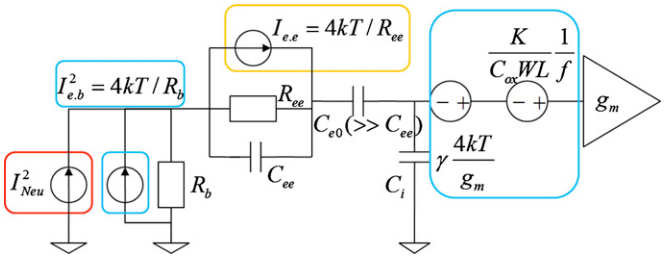

Figure 1. Noise illustration for *in vivo* neural interface: I^2_{Neu} is the lumped neuron noise by background neurons and $I^2_{e.b}$ is lumped tissue/saline thermal noise. Both are modeled as a current source with the seal resistance R_b added in parallel. $I_{e.e}$ is the electrode interface noise produced in a proximity region of the electrode surface [35]. $\gamma\frac{4kT}{g_m}$ is the input referred electronics thermal noise by transistors, switches and resistors. $\frac{K}{C_{ox}WL}\frac{1}{f}$ is the input referred electronics flicker noise produced by transistors [36].

detection errors are not accessible in most experiments, making the topic unsupervised and lacking a benchmark for objective evaluation; neurons and neural networks exhibit nonlinearity and non-stationarity; some spike detection methods rely on waveform shapes [22, 28, 29] and require fine-tuned templates that are difficult to obtain especially in the presence of waveform variation, spike overlapping, recording artifact and interference, and microglia cells that may severely degenerate the signal to noise ratio (SNR).

In this work, we propose a new approach to choose detection threshold. The framework is compatible with many detection algorithms, e.g., spike magnitude, nonlinear energy operator [18, 30], instantaneous energy and waveform slope (derivative). Our focus is to make the algorithm of practical use in different experiment setups and robust to recording imperfections such as waveform variation, spike overlapping, artifact and interference, and low SNR. The rest of this paper is organized as follows. Section 2 focuses on neural interface noise characterization. Section 3 presents algorithms for spike detection. Section 4 presents experimental results. Section 5 gives concluding remarks.

2. *In vivo* neural interface noise characterization

Recorded neural spikes are superimposed with neural interface noise that exhibits non-stationary and non-white-Gaussian characteristics. It can be approximately fitted as $1/f^x$ noise, where f is frequency and x is a positive number less than 3. The frequency dependence is contributed by multiple sources including neuron noise [31–34], electrode–electrolyte interface noise [35], tissue thermal noise and electronic noise [36], which are illustrated in figure 1 using a lumped circuit model. Except the tissue thermal noise ($4kTR_b$ in figure 1) that has a flattened spectrum, the rest decrease with frequency [37].

To verify the neural interface noise contribution from different sources, an *in vivo* experiment is performed that uses two sharp tungsten electrodes separated by 125 μm to record the hippocampus neuronal activities of a rat. One of the electrodes is coated with carbon nanotube (CNT), while the other is uncoated. After the electrodes have been placed, a euthanizing drug is injected. After 5 s of drug injection, the recording of the two electrodes start and last until to the time of death. The noise analysis results are summarized and presented in figure 2. In figure 2(a), a 5 min segment that captures the decaying of background activities is plotted. In figure 2(b), the estimated neural interface noise from 600 Hz to 6 KHz for both recording sites are plotted, where noise dramatically reduces (>80%) after the drug takes effect. Initially, the CNT electrode records a comparatively larger noise (697 μV^2) compared with the uncoated electrode (610 μV^2). After a few minutes, the background noise recorded by the CNT electrode quickly reduces eventually reaching 37 μV^2 that is about 1/3 of noise recorded by its counterpart (112 μV^2), suggesting that the noise floor of using the uncoated tungsten electrode (112 μV^2) is set by the electrode. From these two plots, we can estimate that the neuron noise is around 500–600 μV^2, electrode interface noise is ~80 μV, while the sum of electronic noise and electrolyte bulk noise is less than 37 μV^2 (only ~5% of the neural interface noise). Figure 2(c) displays the $1/f^x$ noise spectrum recorded from the uncoated tungsten electrode ($x = 1.8, 1.4, 1.0, 0.9$, estimated at 0, 15, 30, 45 min after drug injection). Figure 2(d) displays $1/f^x$ noise spectrum recorded from the CNT-coated electrode ($x = 2.1, 1.3, 0.9, 0.8$, estimated at 0, 15, 30, 45 min after drug injection).

Similar experiments have been repeated several times and the results are consistent. Summarized from the experiments, the dominant noise source (>80% reduction) is neuron noise followed by electrode noise. As a follow up to our previous work to characterize contributions from different noise sources [37], in the next session, we study the *in vivo* neural interface noise (the total noise) and its deviation from Gaussian. Since both electrode noise (regardless of the thermal noise model or shot noise model [35]) and circuit noise [36] are Gaussian and they are not the dominant noise sources, without loss of generosity, we sometimes use neuron noise to replace neural interface noise (the summation of neuron noise, electrode noise and circuit noise) in the rest of the paper.

2.1. Neuron noise and central limit theorem

In a generic form, recorded data $V(t)$ are superimposed from spikes, field potentials and neuron noise:

$$V(t) = \sum_{i=1,2,\ldots,I} V_{1,i}(t) + \sum_{j=1,2,\ldots,J} V_{2,j}(t) + V_{\text{syn}}(t) + N_n(t), \tag{1}$$

where $V_{1,i}(t)$ are the activities of a neuron within the recording radius r_1 (spike power is much larger than noise power), $V_{2,j}(t)$ are the activities of a neuron in an extended radius r_2 (spike power is smaller than or comparable to noise power), $V_{\text{syn}}(t)$ is the field potential and $N_n(t)$ is the neural interface noise.

To study neural interface noise and its deviation from Gaussian, histograms of recorded data are shown in figure 3. For broadband data of 1 Hz–8 kHz, the histograms exhibit significant fluctuations as plotted in figure 3(a). The histogram cannot be smoothed by increasing the data length, suggesting data non-stationarity. After applying a high-pass filter at 300 Hz to remove low-frequency activities, data histograms become smoothed and can be approximately fitted by a

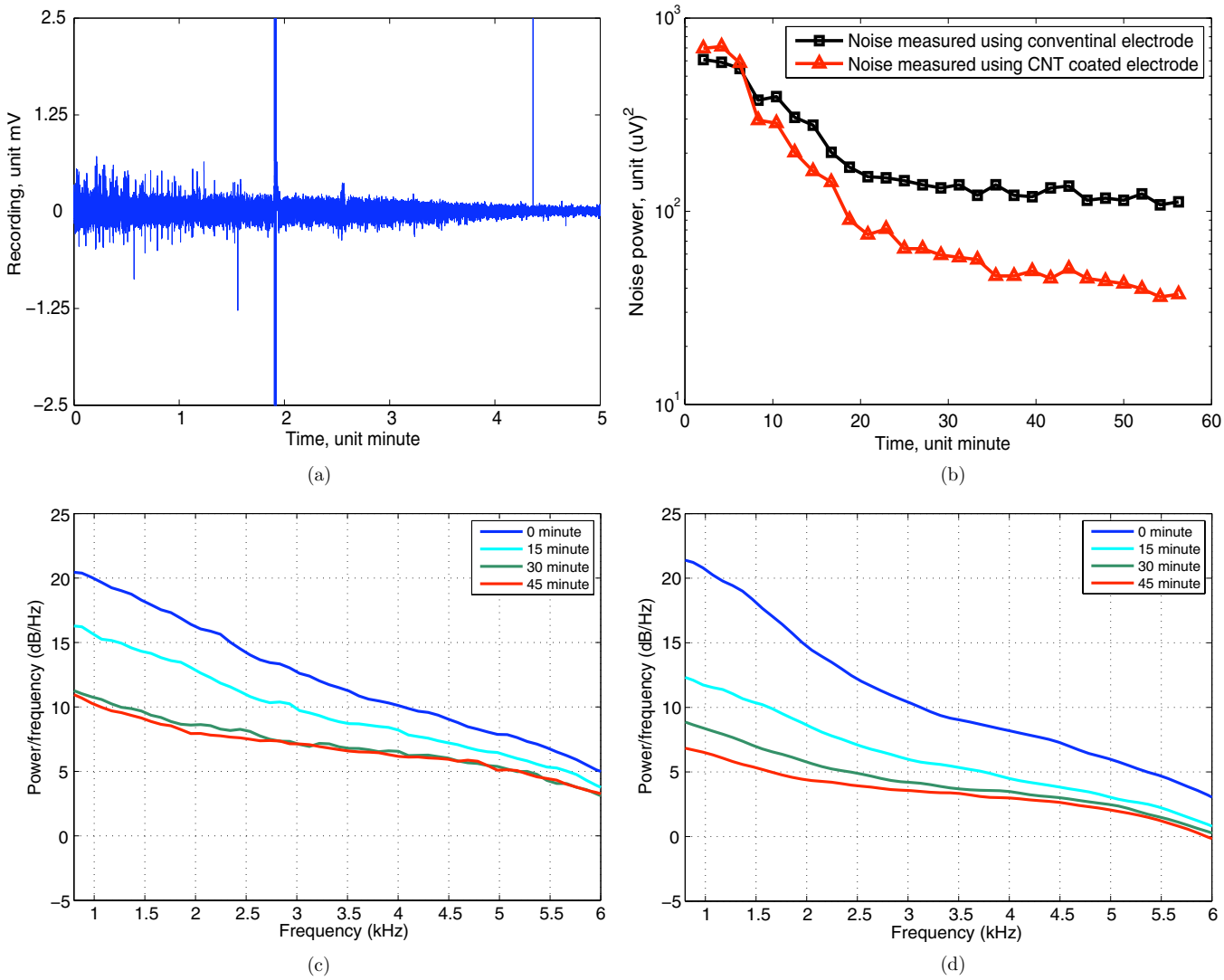

Figure 2. *In vivo* recording for identifying noise sources. (a) Recording segment of 5 min capturing the decay of background activities. (b) Traces of the estimated neural interface noise versus time are plotted. Black ■ curve represents the noise recorded from a custom tungsten electrode; red ▲ curve represents the noise recorded from a CNT-coated electrodes with the same size. (c), (d) Noise power spectrums estimated at the 0, 15, 30, 45 min after the drug injection. In (c), a conventional tungsten electrode is used. A CNT-coated tungsten electrode of equal size is used for comparison (reproduced from [37]) in (d).

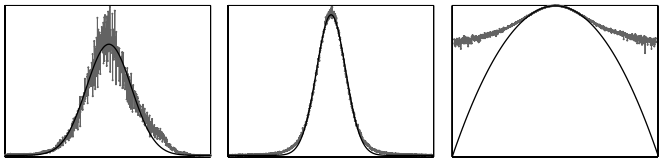

Figure 3. (a) A histogram of broadband neural data at 1 Hz–8 kHz. (b) A histogram of bandpass filtered neural data at 300 Hz–8 kHz. (c) Re-plot of (b) in the log scale.

Gaussian distribution as shown in figure 3(b). The fitting curve excellently matches the histogram at its central region and deviates at regions beyond the data standard deviation (SD) as re-plotted in figure 3(c) in the log scale.

To quantitatively study high-frequency neuron noise, its Gaussian signature and deviations from Gaussian, we refer to the central limit theorem (CLT) [38], which states that the sum of a sufficiently large number of independent random variables, each with identical distribution, finite mean and variance, follows a Gaussian distribution. The conditions of 'independent variables' and 'identical distribution' are strong and more relaxed conditions have been worked out in the literature, e.g., Lyapunov's condition [39] that allows variables of 'different distributions'.

Definition. *Let* X_i, $i = 1, 2, 3, \ldots, K$, *be a sequence of independent random variables. Suppose that each* X_i *has a finite expected value* $E[X_i] = \mu_i$ *and a finite variance* $E[(X_i - \mu_i)^2] = \sigma_i^2$. *If for some* $\delta > 0$, *the expected values* $E[|X_i|^{2+2\delta}]$ *are finite and for every* $1 \leqslant i \leqslant K$,

$$\lim_{K\to\infty} \frac{1}{\left(\sum_{i=1}^{K} \sigma_i^2\right)^{1+\delta}} \sum_{i=1}^{K} E[|X_i - \mu_i|^{2+2\delta}] = 0 \qquad (2)$$

is satisfied, then the convergence to Gaussian holds: $\sum_{i=1}^{K} X_i$ *follows a Gaussian distribution with the mean* $\sum_{i=1}^{K} \mu_i$ *and variance* $\sum_{i=1}^{K} \sigma_i^2$.

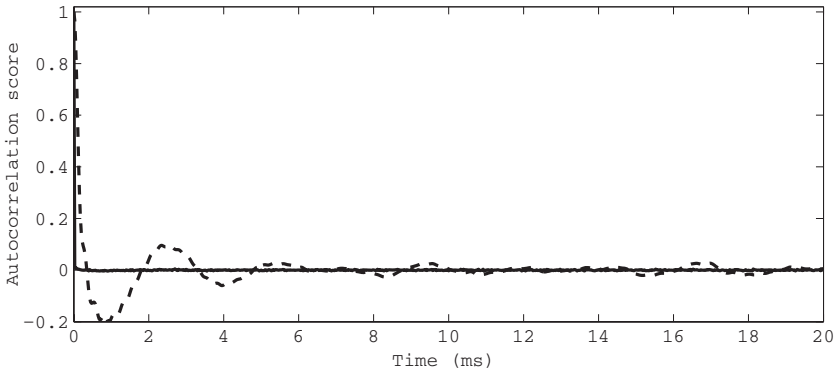

Figure 4. Typical autocorrelation curves of neuron noise (dotted curve) and white Gaussian noise (solid curve). For the sequences that we have tested, the autocorrelation curve has a first zero crossing point around 150–450 μs and stabilized variance in the range from 10^{-6} to 10^{-4}.

If the voltage fluctuation induced by each neuron is treated as a random variable (X_i), then the recorded voltage V is the sum of random variables $V = \sum X_i$ under a framework similar to the CLT. However, there are two issues regarding the application of Lyapunov's condition here. First, mesoscopic-level synchronization positively correlates with the cortical volume enclosed [3], producing long-lasting firing rhythms against the CLT, which explain the deviations from Gaussian in figure 3(a). The synchronized activities appear at less than 200 Hz and can be removed by high-pass filtering. In other words, only a moderate number of neurons located in a proximity region (e.g. a few hundred μm) of the recording site could be treated as the pool for Lyapunov's condition, making the large number hypothesis questionable; it is further added that the convergence to Gaussian is slow: assuming N the number of neurons and a homogeneous neuron density function, we derive that equation (2) converges at a rate of $O(N^{1/3})$. Second, the strength of pairwise synchronization is inversely proportional to the distance between the neurons [1], implying that the random variables to be summed over are not completely independent. A relaxation on the requirement of independence is possible for the CLT [40, 41]; however, it still lacks a sufficient and necessary condition. Alternatively, we have analyzed sequences collected from different animal preparations to investigate the validity of CLT. As an example shown in figure 4, after being high-pass filtered at 300 Hz, typical autocorrelation curves of neural interface noise have their first zero-crossing point around a few hundred μs. The waveform ripples decay very fast initially and approach a slowly decaying state with the variance 10^{-6}–10^{-4}, suggesting a weak but a long-lasting correlation among samples. The data histograms, on the other hand, exhibit small deviations from Gaussian. In section 3, we reason that the small deviations are caused by sparse distribution of spike energy: neuronal synchronization breaks the hypothesis of independence (field potentials, figure 3(a)), while a number of nearby, high firing-rate neurons (neural spikes, figures 3(b) and (c)) violate Lyapunov's conditions.

3. Unsupervised near-optimal neural spike detection

In this section, we propose a framework for estimating the spike detection threshold. As shown in sections 3.1 and 3.2, a transformation of neural data to its analytic form reveals two statistical components: an exponential term caused by the regulation of CLT (neuron noise) and a power term caused by the violation of Lyapunov's condition (spikes). In sections 3.3 and 3.4, a threshold estimation method is proposed based on these two components.

3.1. Neural interface noise—exponential component

Definition. *A real sequence $V(t)$ (neural data) and its Hilbert transform $HV(t)$ are related to each other that they together form a strong analytic signal $V_{\rm st}(t)$ [42–44]:*

$$V_{\rm st}(t) = V(t) + {\rm i}HV(t) = V(t) + {\rm i}\frac{1}{\pi}P\int_{-\infty}^{\infty}\frac{V(\tau)}{t-\tau}\,{\rm d}\tau, \quad (3)$$

where P in front of the integral denotes the Cauchy principal value and H denotes the Hilbert transform.

We choose to detect neural spikes based on the analytic signal $|V_{\rm st}(t)| = \sqrt{V(t)^2 + HV(t)^2}$ rather than $V(t)$ (although they are approximately equivalent) for two reasons. First, extracellular spike could have significant variation in shape; sometimes they may require multiple detection windows of different thresholds. As a comparison, the corresponding analytic signal (square root of instantaneous energy) has less variation in shape and only require a single threshold for different shaped spikes, as illustrated in figure 5. Second, as to be derived here, background noise has a simple representation in Hilbert space. Denote the discrete versions of $V(t)$ and $HV(t)$ as $V(m\Delta T)$ and $HV(m\Delta T)$, where $m = \ldots, -1, 0, 1, 2, \ldots$ and ΔT is the sampling interval. By definition, $HV(m\Delta T)$ is a weighted sum of a series of correlated Gaussian random variables that approximately converges to Gaussian. The dependence between $V(m\Delta T)$ and $HV(m\Delta T)$ can be quantified through a modified cosine similarity Y_V (from completely independent to dependent, Y_V increases from 0 to 1):

$$Y_V = \left|1 - \frac{\int_{-\infty}^{\infty} f_V(x_1) f_{HV}(x_2) f_{V,HV}(x_1, x_2)\,{\rm d}x_1\,{\rm d}x_2}{\int_{-\infty}^{\infty} f_{V,HV}^2(x_1, x_2)\,{\rm d}x_1\,{\rm d}x_2}\right|, \quad (4)$$

where f_V and f_{HV} are the density functions of $V(m\Delta T)$ and $HV(m\Delta T)$, respectively; $f_{V,HV}$ is the joint density function. Measured results based on *in vivo* data show that Y_V is in a range from 0.0007 (associated with inactive states, e.g.,

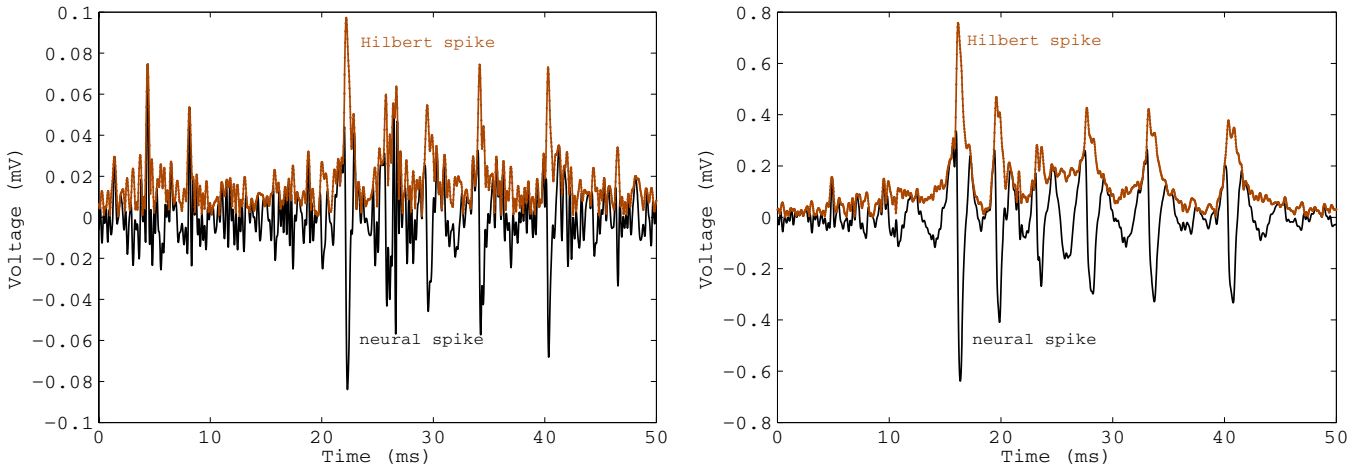

Figure 5. Neural spike data (black) and their analytic waveforms (brown). (a) A burst of spikes with 1–2 ms width and 100 μV magnitude. (b) A burst of spikes with 2–4 ms width and 1 mV magnitude. Waveforms in both (a) and (b) are picked from a same recorded sequence with 3 s of separation.

figure 6(a)) to 0.035 (associated with active states, e.g., figure 6(b)), suggesting that $\{HV(m\Delta T)\}$ and $\{V(m\Delta T)\}$ are nearly independent Gaussian variables. Added that the Hilbert transform does not change the signal power, it gives the following property of neuron noise: define $Z(m\Delta T)$ the power of analytic signal $V_{\rm st}(m\Delta T)$, and the cumulative probability function of Z is

$$F(Z_0) = \Pr[Z < Z_0] = \int_{-\sqrt{Z_0}}^{\sqrt{Z_0}} \int_{-\sqrt{Z_0-y^2}}^{\sqrt{Z_0-y^2}} f_{V,HV}(x,y)\,\mathrm{d}x\,\mathrm{d}y,$$
$$\approx \int_{-\sqrt{Z_0}}^{\sqrt{Z_0}} \int_{-\sqrt{Z_0-y^2}}^{\sqrt{Z_0-y^2}} f_V(x) f_{HV}(y)\,\mathrm{d}x\,\mathrm{d}y = 1 - \mathrm{e}^{-\frac{Z_0}{2\sigma_n^2}}, \tag{5}$$

where $F(Z_0)$ is the cumulative probability function with respect to the instantaneous signal power Z_0 and σ_n is the SD of background noise.

Equation (5) gives a clear description of high-pass filtered (>300 Hz) noise generated by background neurons: in the linear-log scale, the probability density function (pdf) $f(Z_0) = \frac{\mathrm{dPr}(Z<Z_0)}{\mathrm{d}Z_0}$ is a straight line with a slope equal to $-\frac{1}{2\sigma^2}$ (the square of a Rayleigh distribution in [16]). In other words, there exist detectable neural spikes that invalidate equation (2) (detailed in section 3.2), if $f(Z_0)$ deviates from a straight line or with a different slope (detectable neural spikes increase the slope); and this deviation positively correlates with the spikes frequency.

3.2. Neural spikes—power-law component

As discussed in section 3.1, neuron noise gives the signal instantaneous power Z an exponential density function $f(Z)$, while the presence of 'neural spikes' makes $f(Z)$ to deviate from the exponential form. In this section, emphasis is made to reason that large magnitude, fast rate spikes violate Lyapunov's condition and make the deviation a power-law component.

We first examine the validity of Lyapunov's condition (equation (2)) in the context of neural recording:

$$\Theta = \lim_{N\to\infty} \frac{1}{\left(\sum_{i=1}^{N}\sigma_i^2\right)^{1+\delta}} \sum_{i=1}^{N} E[|X_i-\mu_i|^{2+2\delta}]$$
$$> \left(\frac{\sigma_L}{\sigma}\right)^{2+\delta} \frac{T_L r_L}{f_s} \quad \forall L, \tag{6}$$

where Θ is a parameter to quantify the validity of Lyapunov's condition (a smaller Θ suggests Lyapunov's condition holds better); L is used to identify the variable of the largest variance (large spikes), T_L is the spike width, r_L is the firing rate, f_s is the sampling frequency, σ^2 is neural data variance and σ_L^2 represents the spike variance within the waveform window. If we assume a homogeneous neuron density and independent firings, Θ converges to 0 as N increases. However, the convergence rate is slower than linear ($\sim N^{1/3}$). The slow convergence makes the validity of Lyapunov's condition to rely on a hypothesis of small variance of each individual variable, which is proportional to its firing rate and induced spike power. As an example shown in figure 6(a), spikes are large in magnitude and low in frequency, making Θ in equation (6) small. Consequently, Z follows an exponential distribution $f(Z) = 10^{-1.7}\,\mathrm{e}^{-0.503Z}$. As a comparison shown in figure 6(c), spikes have a large magnitude and high firing rates, which degenerate Lyapunov's condition; as a result, $f(Z)$ deviates from an exponential distribution as plotted in figure 6(d). In the following, we quantitatively investigate this deviation.

Following equation (1), the analytic signal of recorded neural data $V_a(m\Delta T)$ is

$$V_a(m\Delta T) = \left[\sum_{i=1}^{A} V_{s,i}(m\Delta T) + N(m\Delta T)\right],$$
$$+\mathrm{i}\left[H\sum_{i=1}^{A} V_{s,i}(m\Delta T) + HN(m\Delta T)\right], \tag{7}$$

where $V_{s,i}(m\Delta T)$ and $N(m\Delta T)$ are neural spikes and neuron noise, respectively, and A is used to note a set of neurons that induce detectable spikes.

Denote as M the magnitude of a spike ($M > \sigma_n$, σ_n is the neuron noise SD calculated from $N(m\Delta T)$), by Coulomb's

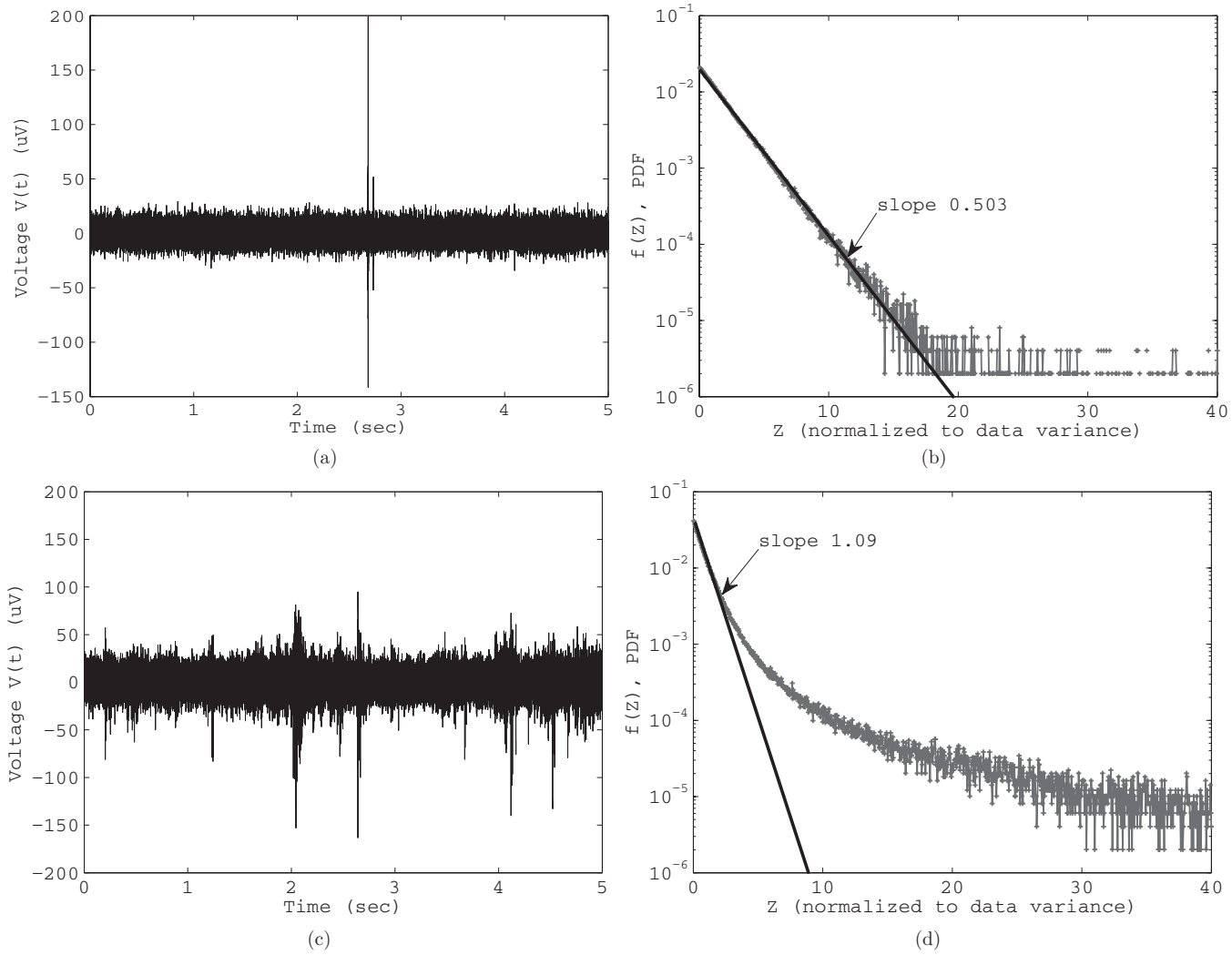

Figure 6. (a) Neural data with a small amount of visually detectable spikes (differentiable from background activates). (b) Measured pdf of data in (a) is fitted by an exponential function over four orders. The x-axis: Z normalized to data variance (scaled by $1/\sigma^2$). The vertical axis: pdf in the log scale. $f(Z) = 10^{-1.7}\mathrm{e}^{-0.503Z}$ compared with the theoretical prediction $f(Z) = 10^{-1.7}\mathrm{e}^{-0.5Z}$. (c) Neural data with more visually detectable spikes. (d) Measured pdf in (c), which deviates from an exponential distribution as Z increases. For $Z < 3$, $f(Z) = 10^{-1.4}\mathrm{e}^{-1.09Z}$. For all the experiments shown in this paper, $f(Z)$ is quantized as 10^{-6}. This causes scattering at the tail as shown in (b) and (d).

law; M is inversely proportional to the distance between the source (neuron) and the measuring point (electrode). Based on this property, the pdf of the number of neurons with respect to M, $\rho(M)$, is

$$\rho(M) = cr(M)^2 \left|\frac{\mathrm{d}r(M)}{\mathrm{d}M}\right| \propto M^{-4}, \tag{8}$$

where c is a constant relating to neuron density (number of neurons per mm^3), and $r(M)$ is the distance from a targeted neuron to the recording site.

Assume that an analytic spike of magnitude M introduces W equally spaced samples on average $\left(W \approx \frac{T_L}{\Delta T}\right)$, based on equation (8), the density function of spike power $f_d(Z)$ is

$$f_d(Z) \approx \left[\int_s^{+\infty} \rho(M)\frac{W}{M}\,\mathrm{d}M\right]\frac{\mathrm{d}s}{\mathrm{d}Z}|_{s=Z^{0.5}, Z\gg\sigma_n} \propto \frac{1}{Z^{2.5}}, \tag{9}$$

where $f_d(Z)$ is the added component by neural spikes, causing $f(Z)$ to deviate from Gaussian.

Combine equations (5) and (9); $f(Z)$ is a combination of an exponential component ($e^{-\lambda_1 Z}$, EC) and a power-law component ($Z^{-\lambda_2}$, PC): $e^{-\lambda_1 Z}$ is caused by background noise regulated by the CLT, and $Z^{-\lambda_2}$ is caused by detectable spikes that violate Lyapunov's condition of small variance of individual variables. Typical results derived from *in vivo* data are shown in figure 7, which clearly confirm the existence of both $\mathrm{e}^{-\lambda_1 Z}$ and $Z^{-\lambda_2}$.

3.3. Threshold estimation

Assume $\widetilde{f}_n(Z)$ and $\widetilde{f}_d(Z)$ the exponential component and the power-law component trained in real-time, and $f(Z) = \widetilde{f}_n(Z) + \widetilde{f}_d(Z)$, $\int_0^\infty f(Z)\,\mathrm{d}Z = 1$. Given a sample $Z(m\Delta T) = Z_0$, the probability of the presence of a spike $p_s(m\Delta T)$ can be quantitatively accessed, e.g., using the maximum-likelihood estimation:

$$p_s(m\Delta T) = \frac{\widetilde{f}_d(Z_0)}{\widetilde{f}_d(Z_0) + \widetilde{f}_n(Z_0)}|_{Z_0 = V(m\Delta T)^2 + HV(m\Delta T)^2}. \tag{10}$$

As discussed in section 1, a quantitative evaluation of threshold requires the benchmark as *a priori* that is not

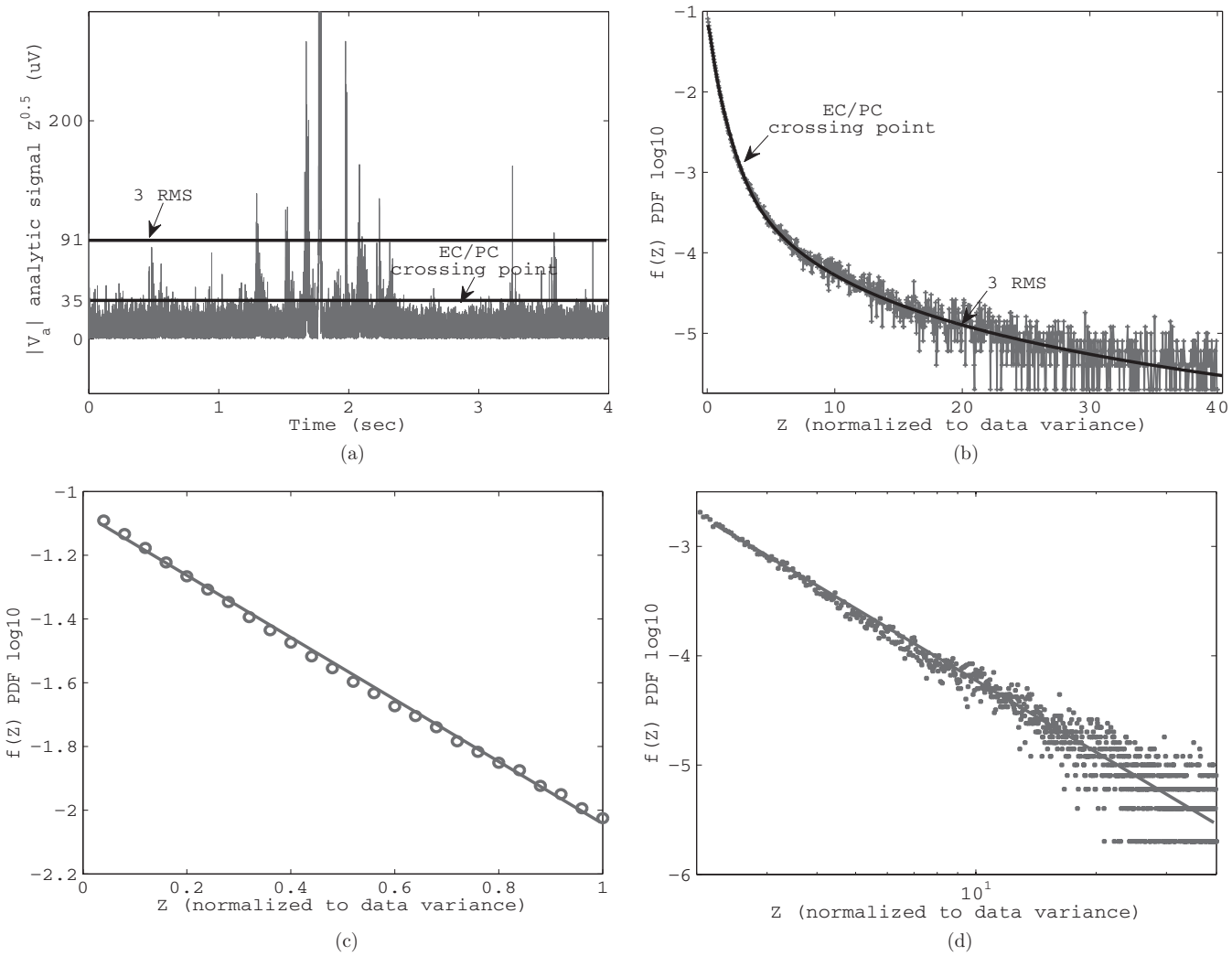

Figure 7. (a) Analytic waveforms of recorded data with thresholds labeled for comparison. (b) Pdf of analytic signal power $f(Z)$. For this sequence, the crossing point of $e^{-\lambda_1 Z}$ and $Z^{-\lambda_2}$ (EC/PC) suggests over 30 times increased spike events compared with using 3×RMS threshold. (c) When $Z/\sigma^2 < 1$, $e^{-\lambda_1 Z}$ dominates $Z^{-\lambda_2}$; therefore, $f(Z)$ is fitted by an exponential trace in the log scale. (d) As Z increases, $Z^{-\lambda_2}$ dominates $e^{-\lambda_1 Z}$, and $f(Z)$ is fitted by a power component in the log–log scale.

available. $p_s(m\Delta T)$ in equation (10) can be used as a replacement of the benchmark. The optimal threshold is the one that generates spike firing patterns matching $p_s(m\Delta T)$ most: given a segmentation scheme of neural data $w_k, k = 1, 2, 3, \ldots$, and a threshold, the detected spike patterns are noted as $P_{\text{th}}(k)$. An integration procedure over $p_s(m\Delta T)$ is applied over the same segmentation scheme; in this work, we use a simple winner-take-all strategy that captures the peak instantaneous energy regardless of the waveform width

$$P_s(k) = \underset{m\in[w_k, w_{k+1}]}{\text{Max}} \{p_s(m\Delta T)\}, \tag{11}$$

where $P_s(k)$ is the probability that a spike appears in the kth segment and an optimal detection threshold is the one that maximizes the similarity between $P_s(k)$ and $P_{\text{th}}(k)$.

3.4. Step-by-step algorithm recipe

A step-by-step algorithm explanation correlated with algorithm flow shown in figure 8 are given as follows.

Data preparation: high pass filtering raw data at 300 Hz to remove low frequency activities. Filtered data are noted as $V(t)$, which are contributed by a large number of background neurons.

Step 1. Applying the Hilbert transform to the high pass filtered neural data $V(t)$ as shown in equation (3). According to equations (3)–(5), neuron noise has an exponential distribution $e^{-\frac{Z}{2\sigma_n^2}}$, where σ_n^2 is the noise variance and Z is the instantaneous energy in Hilbert space. Because noise variance is always smaller than the data variance σ^2, thus the exponential distribution takes a general form $e^{-\lambda_1 Z}$ with $\lambda_1 \geqslant \frac{1}{2\sigma^2}$.

According to equations (6) to (9), detectable neural spikes generate a power-law distribution $Z^{-\lambda_2}$. It can be attributed to violations of Lyapunov's conditions: some neurons are more close to the electrode and induce large spikes that invalidate the hypothesis of small variance of individual variables. The induced spike magnitude is inversely proportional to the distance between the neuron and the electrode, and consequently, detectable neural spikes give a power-law distribution. In the ideal case that neurons are homogenously distributed and each with equal transmembrane current density, the distribution follows $Z^{-2.5}$.

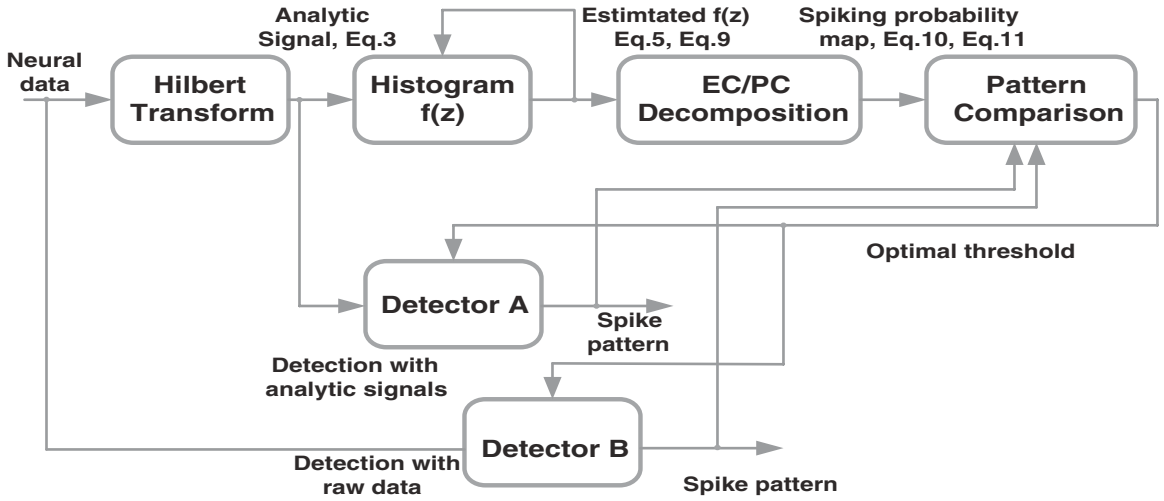

Figure 8. Step-by-step flow of the proposed spike detection algorithm.

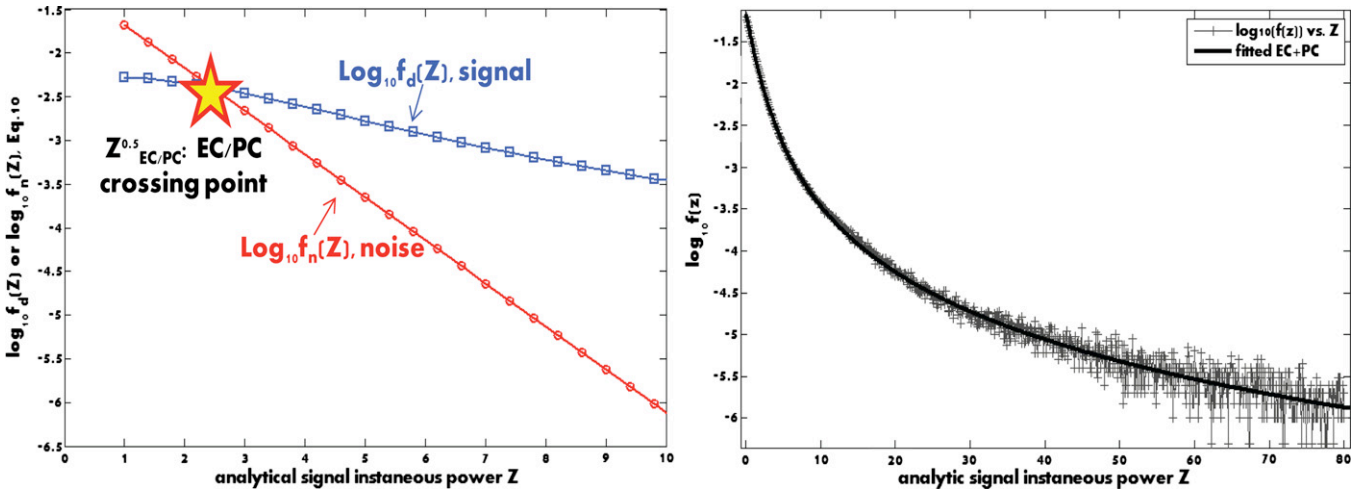

Figure 9. (left) EC/PC decomposition. The x-axis is signal power normalized data variance; the y-axis is the probability in $\log_{10}$. Red (circle) line is an inferred EC (noise) and blue (square) line is an inferred PC (signal). (right) Superimposed EC+PC in comparison with neural data energy distribution ($f(Z)$).

Step 2. Applying a linear decomposition algorithm to separate $f(Z)$ into two components, $\widetilde{f}_n(Z) \sim e^{-\lambda_1 Z}$ (noise) and $\widetilde{f}_d(Z) \sim \frac{1}{a+Z^{\lambda_2}} \approx Z^{-\lambda_2}$ (signal). For $\widetilde{f}_d(Z)$, the regulation at small Z is because the noise variance σ_n^2 implicitly sets a lower boundary for s in equation (9). In other words, if the magnitude of induced spikes is too small, spikes contribute to background noise and cannot be reliably detected. A snapshot of typical components decomposition results is shown in figure 9.

Step 3. Generating a 'spiking probability map' P_s based on equations (10) and (11). The estimated $\widetilde{f}_n$ and $\widetilde{f}_d(Z)$ are the input. The 'spiking probability' refers to the chance of the presence of a spike at a given time, as shown in figure 10.

Step 4. Choosing a spike detection threshold based on the generated 'spiking probability map'. The user can choose detection threshold based on the spiking probability, e.g., 80%. (On average, 80 out 100 detected spikes are true spikes. The rest 20 are from noise.) Or alternatively, the user can calculate an optimal threshold that gives the maximal temporal similarity between the detection results (1/0 pattern) and the spiking probability map.

4. Data analysis results

In section 4.1, we use animal data to argue that the estimated detection threshold correlates with the background spiking activities. Furthermore, we report that there are substantial variations in estimated detection threshold for (1) data recorded from the same channel but at different time slots and (2) data recorded from different channels at the same time.

In section 4.2, we use synthesized data to quantitatively evaluate the algorithm performance. We report that the proposed algorithm can predict receiver operator characteristics (ROC) curves that are almost identical to benchmarks. The results confirm that the proposed spiking probability map can be used for choosing detection threshold. Finally, quantitative comparisons between the predicted

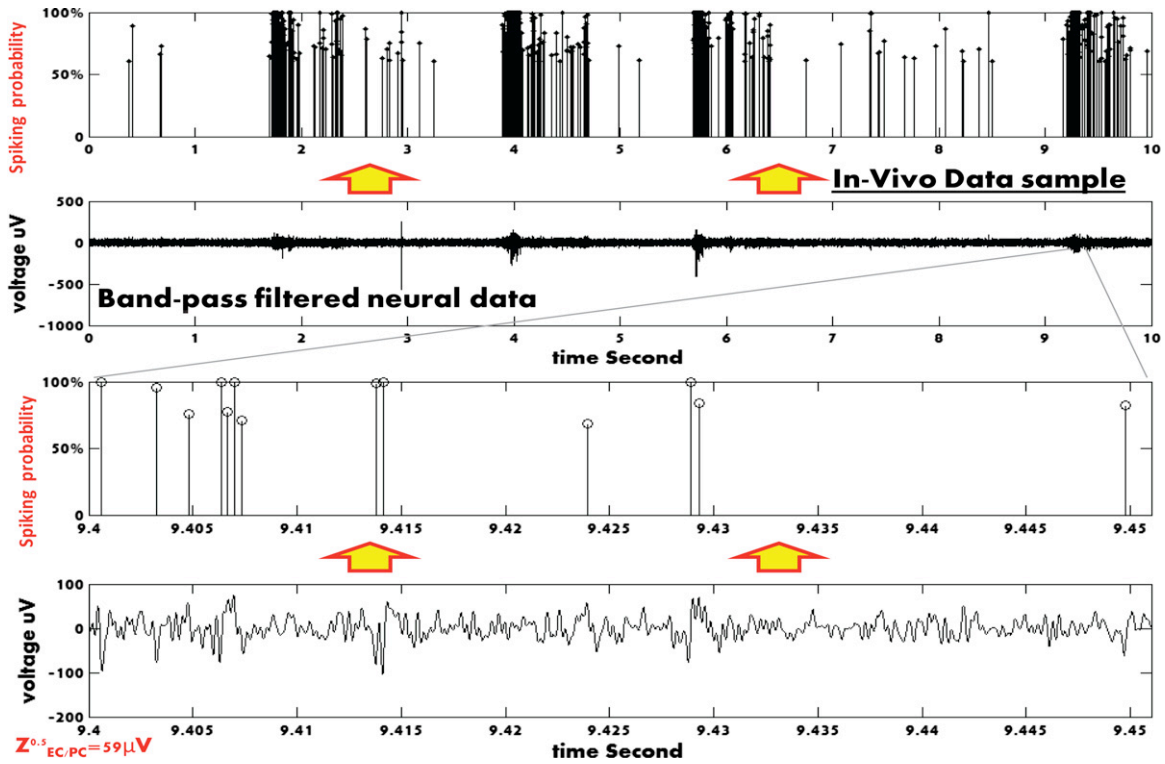

Figure 10. Spiking probability map in comparison with neural data. The *x*-axis time in second. First trace: spiking probability map in 10 s window. Second trace: neural data high pass filtered at 300 Hz. Third trace: spiking probability map in 50 ms window (9.4–9.45 s). Fourth trace: the corresponding spike data in the 50 ms window.

spiking probabilities and measured probabilities are included to validate the algorithm prediction accuracy.

4.1. Validation using experimental in vivo animal data

4.1.1. Validation of two statistical components. Testing results on 109 *in vivo* sequences are summarized in figure 11. The data are independently recorded from hippocampus, cortex surface and spinal cord; both acute and long-term recordings; and sleep and awake states. Typical *in vivo* neural data illustrating different firing rates, on/off duties and SNR (defined as spike amplitude divided by noise RMS) are shown in figure 12 along with the corresponding EC/PC decomposition results. Over ∼30% sequences tested (an example is shown in figure 7), a threshold near the crossing point of $e^{-\lambda_1 Z}$ and $Z^{-\lambda_2}$ (EC/PC) gives >10 times more spikes than 3×RMS does, suggesting a large headroom for increasing information capacity.

On all 109 sequences tested, λ_1/σ^2 is averaged to be 0.7719 ± 0.5082, as shown in figure 11(a). The histogram of λ_1/σ^2 clearly peaks at '0.5', which is consistent with the prediction by equation (5). A power component $Z^{-\lambda_2}$ has been observed in all the sequences. As summarized in figure 11(b), $\lambda_2 = 2.516 \pm 0.564$ astonishingly matches the predicted '2.5' by equation (9). The model fitting of $f(Z)$ using $e^{-\lambda_1 Z}$ and $Z^{-\lambda_2}$ in the log scale have passed statistical validations: the repeatability measured by R^2 score [45] is $99.56 \pm 0.14\%$; the accuracy measured by the root mean square deviation (RMSD) is 0.056 ± 0.014. As summarized in figures 11(c) and (d), the estimated optimal threshold exhibits significant variations from 23 to 155 μV.

4.1.2. EC/PC crossing point variation over time. As illustrated in figure 13(a)–(c), $Z^{0.5}_{EC/PC}$ (the predicted threshold that corresponds to 50% correct detections and 50% false detections) versus time traces are plotted, where data are recorded from hippocampus, cortex and cortex superficial layer. We find out in some cases $Z^{0.5}_{EC/PC}$ does not change much (<30%) over time, e.g., figures 13(a) and (b); while in some other cases, $Z^{0.5}_{EC/PC}$ may change suddenly, e.g., figure 13(c). Our experiments confirm that $Z^{0.5}_{EC/PC}$ well tracks spiking activities: when spiking activities are frequent and differentiable from noise (a high SNR), $Z^{0.5}_{EC/PC}$ tends to be lower than 2.5 (Figure 13(a)). When spiking activities are infrequent, $Z^{0.5}_{EC/PC}$ tends to be higher (Figure 13(c) and (f)). The results here are consistent with the prediction that when individual neural spikes with variances comparable to the background data RMS, Θ in equation (10) is a small number ($\ll 1$) and neural spikes merge to background noise according to Lyapunov's condition. In this case, an optimal detection threshold will be biased to reduce the false alarm according to the maximum-likelihood criterion, and thus a larger $Z^{0.5}_{EC/PC}$. When neurons induce frequent and large magnitude spikes, Θ in equation (10) becomes larger and neural activities form a new distribution (PC in Hilbert space). In this case, the neural data RMS should be notably larger than the background noise RMS, and thus $Z^{0.5}_{EC/PC}$ is smaller.

As shown in figures 13(c) and (f), $Z^{0.5}_{EC/PC}$ may change over time. If $Z^{0.5}_{EC/PC}$ is indeed coupled with the optimal detection

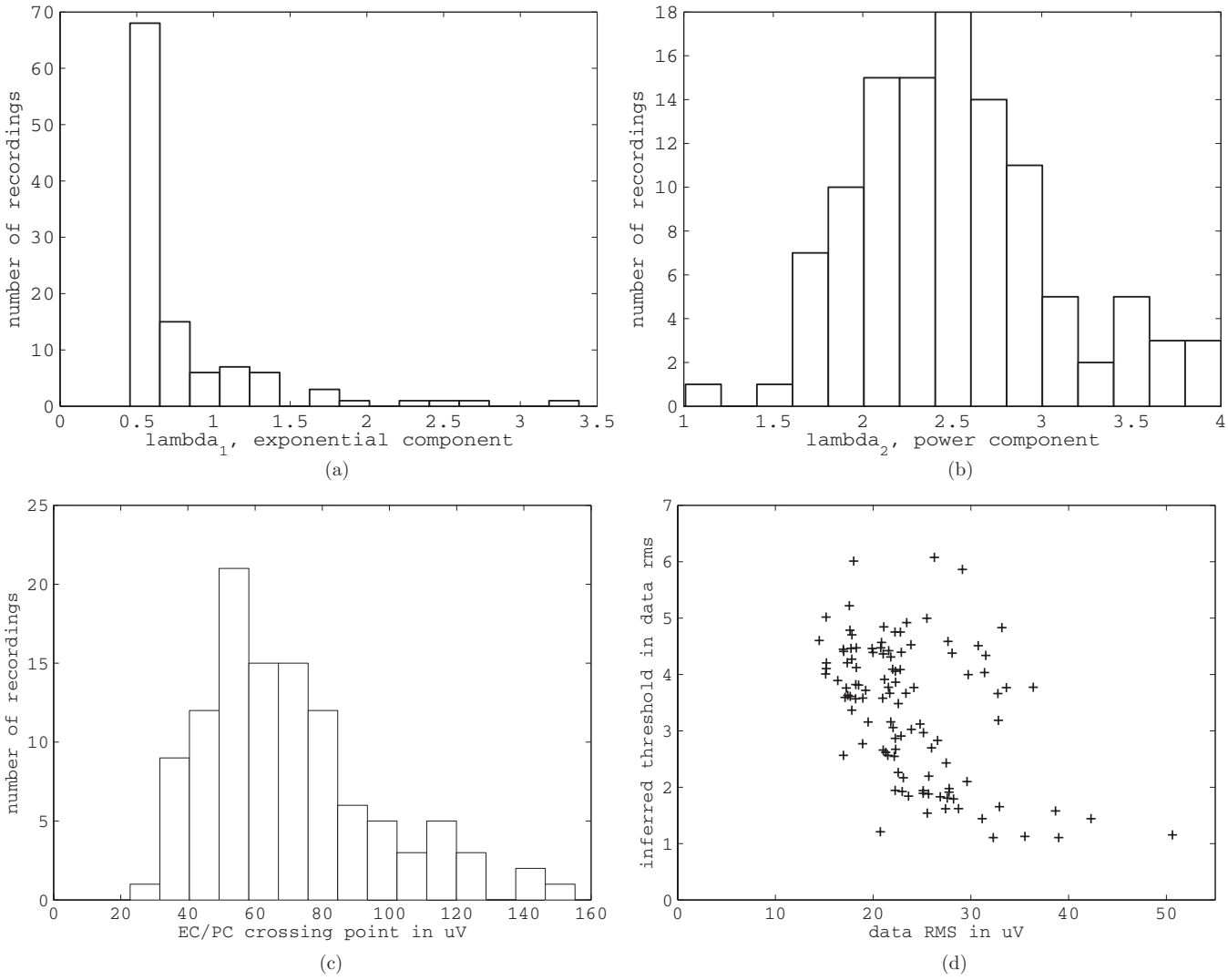

Figure 11. (a) Measured histogram of λ_1/σ^2. As predicted by equation (5), it peaks at 0.5. (b) Measured histogram of λ_2, astonishingly matching the predicted 2.5 by equation (9). (c) Histogram of EC/PC crossing point ($Z^{0.5}$) in μV. (d) Estimated threshold; x-axis: data SD in μV, and y-axis: estimated optimal threshold referred to as σ (Z/σ^2). Data statistics are derived from 109/109 *in vivo* recordings contributed from independent experiments: $\lambda_1/\sigma^2 = 0.7719 \pm 0.5082$, $\lambda_2 = 2.516 \pm 0.564$, $R^2 = 99.56 \pm 0.14\%$ (repeatability), RMSD $= 0.056 \pm 0.014$ (accuracy). $f(Z)$ is quantized at a resolution of 10^{-5}.

threshold, it requires algorithms to constantly update the detection threshold. A sequence that has a sudden change in $Z^{0.5}_{\mathrm{EC/PC}}$ is shown in figure 14(a), where $Z^{0.5}_{\mathrm{EC/PC}}$ initially fluctuates around 3.5 and suddenly drops to around 2 at 330 s time marker. For a clear comparison, recorded data segments at 0–50, 320–350 and 400–450 s are plotted in figures 14(b)–(d) respectively. When spikes are less visually differentiable from the background activities as shown in figure 14(b), $Z^{0.5}_{\mathrm{EC/PC}}$ scores higher, which suggests a smaller number of detectable spikes. From the transition of less differentiable to more differentiable spiking activities as shown in figure 14(c), $Z^{0.5}_{\mathrm{EC/PC}}$ drops from 3.5 to 2, which confirms an increased number of detectable spikes. When there are sustained spiking activities (400–700 s) as shown in figure 14(d), $Z^{0.5}_{\mathrm{EC/PC}}$ remains a lower score around 2.5. Results presented in figure 14 shows that $Z^{0.5}_{\mathrm{EC/PC}}$ is a good indicator of the background activities and coupled with the spike detection threshold.

To investigate $Z^{0.5}_{\mathrm{EC/PC}}$ statistics over different recording channels, multi-channel recording experiments are performed using the Plexon system with 1–8000 Hz bandwidth on the amplifiers. Adjacent electrodes are separated by 150 μm to allow studying the spatial sensitivity of $Z^{0.5}_{\mathrm{EC/PC}}$. Figure 15 summarizes derived $Z^{0.5}_{\mathrm{EC/PC}}$ at different channels and different trails: each row is one trail that consists of five channels. Experiment data suggest that there exists substantial variation in $Z^{0.5}_{\mathrm{EC/PC}}$ among different recording channels (even two adjacent channels), and thus independent threshold estimation should be performed for different channels.

4.2. Validation using synthesized data

4.2.1. Prediction 50%–50% threshold. To quantitatively evaluate the proposed detection algorithm, we have prepared a synthesized data base to mimic real recordings. As illustrated in figure 16, recorded *in vivo* data that contain a small number

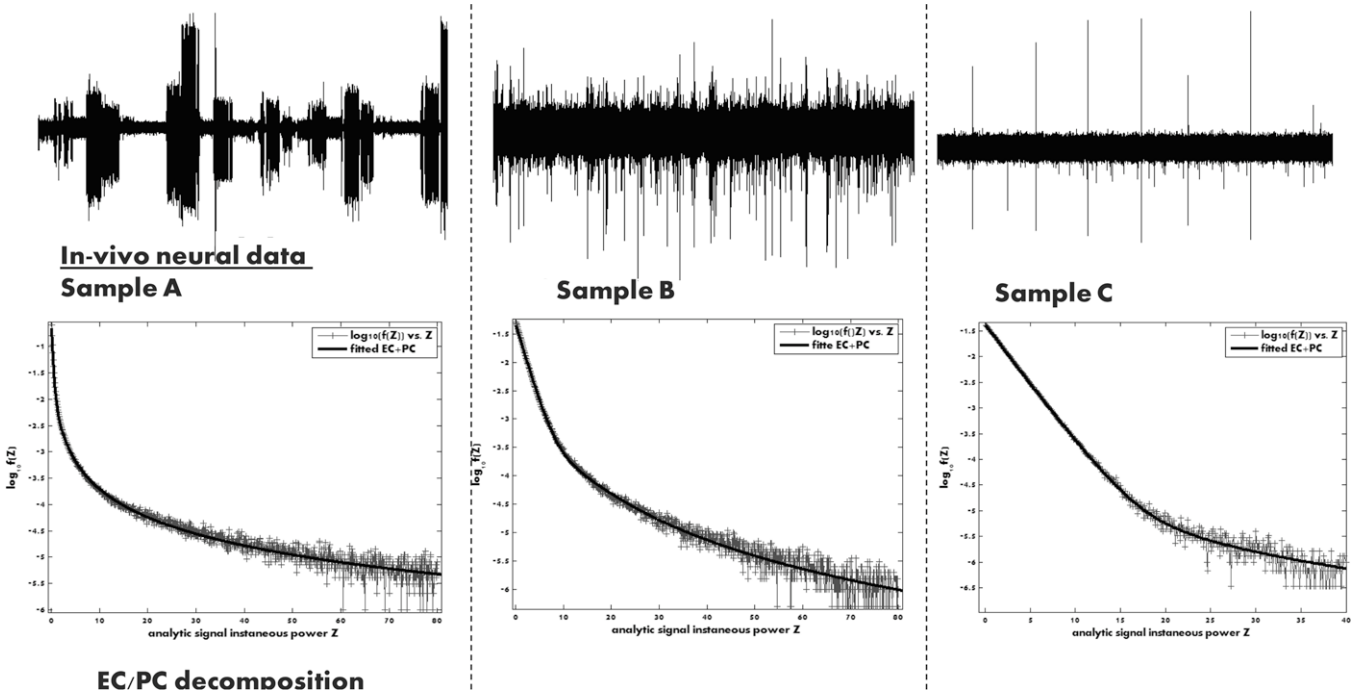

Figure 12. Sampled *in vivo* data segment (upper figures) and their corresponding EC/PC decomposition (bottom figures).

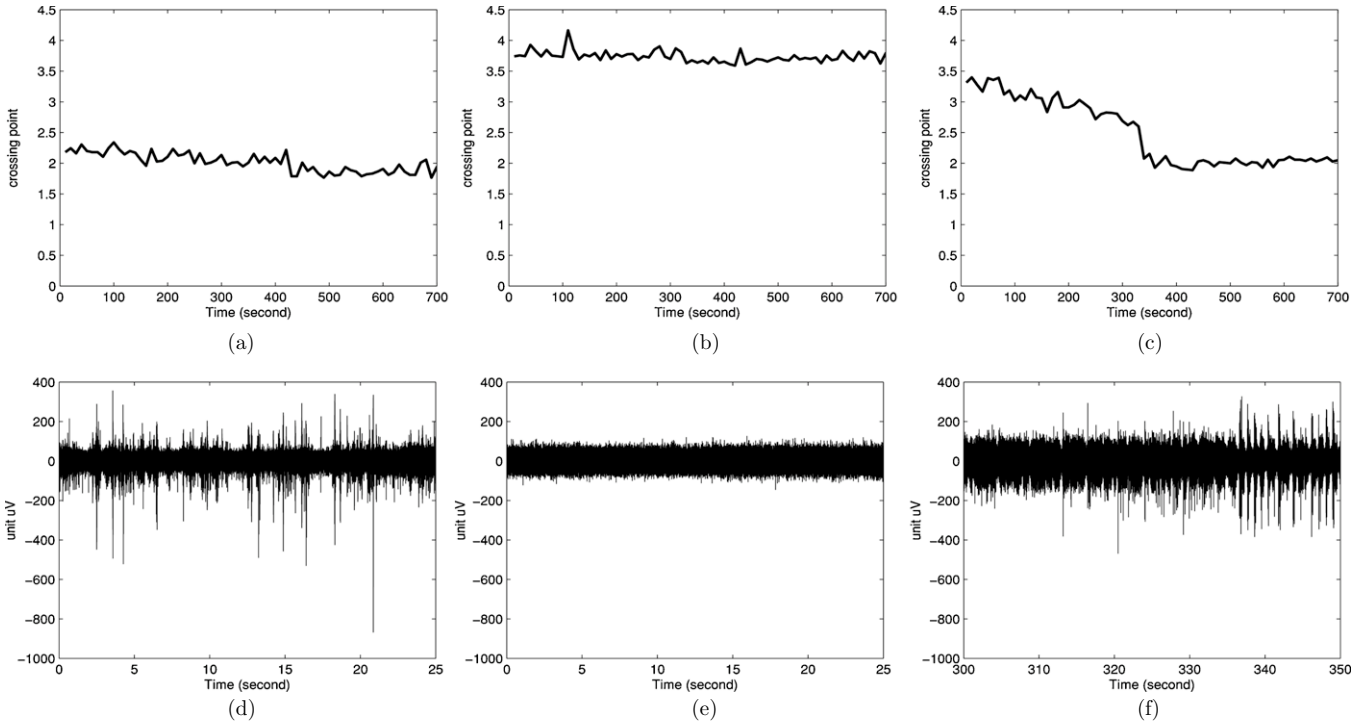

Figure 13. (a)–(c) EC/PC crossing point ($Z^{0.5}_{EC/PC}$) versus time. The *x*-axis is time, and the *y*-axis is the EC/PC crossing point normalized to data rms. A bandpass filter of 300 Hz–8 kHz has been applied to calculate the data rms. (d)–(f) Sampled data segments, where (a)–(c) have one-to-one correspondence to (d)–(f). For a segment that includes more visually detectable spikes, $Z^{0.5}_{EC/PC}$ is smaller (<2.5).

of visually detectable spikes are used as the background noise; recorded spike waveforms with a large magnitude (>500 μV) are used to model the shapes of neural spikes. Independent neurons of varied transmembrane current magnitudes (to model variations in axonal radius and ion channel density) are randomly added within a few hundred μm radius of a point electrode. The induced spikes attenuate according to the distance to the electrode. The amplitudes of added neurons are in a wide range from 5 μV (small and distant neurons, more likely to appear) to 1.3 mV (large and close neurons, less likely to appear). The maximal number of neurons added in this simulation is 50, allowing overlapping spikes. Neurons' firings are assumed to follow the inhomogeneous Poisson process with varied on/off firing states; the averaged firing

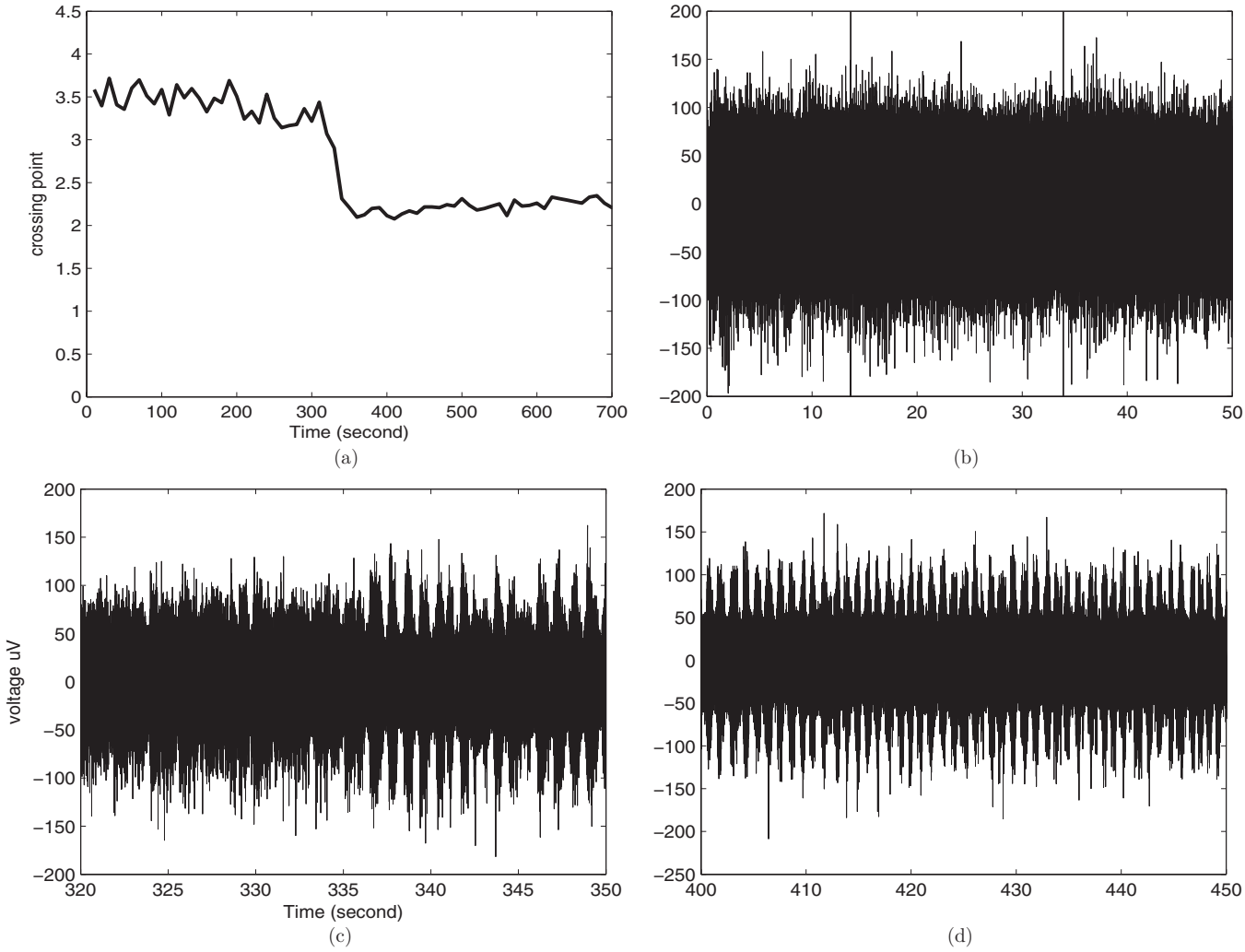

Figure 14. (a) $Z^{0.5}_{\mathrm{EC/PC}}$ versus time, where there is a sudden step-down during 300–350 s time marker. (b) Bandpass filtered neural data at 300 Hz–8 kHz during 0–50 s time marker, where there are less visually detectable spikes. (c) Bandpass filtered neural data during 300–350 s time marker, where there is a sudden increase in spiking activities starting at 335 s time marker. The change in spiking rate is coupled with $Z^{0.5}_{\mathrm{EC/PC}}$ as shown in (a). (d) Bandpass filtered neural data in 400–500 s, which have shown sustained high-rate spiking activities.

rates are randomly picked from 0.1 to 10 Hz. The rest of neurons are assumed to fire a train of spikes each time with the 2 mS refractory period.

Figure 17 displays the predicted EC/PC crossing point $Z^{0.5}_{\mathrm{EC/PC}}$ (x-axis) compared with the measured threshold $V_{T.50\%}$ (y-axis) that incurs 50% correct detections and 50% false detections: $Z^{0.5}_{\mathrm{EC/PC}}$ is predicted by equation (10); $V_{T.50\%}$ is obtained by sweeping the detection threshold and comparing results with the benchmark. According to equation (10), $V_{T.50\%}$ should be very close to $Z^{0.5}_{\mathrm{EC/PC}}$ due to an exponential sensitivity of equation (10) around 0.5. The fitting results summarized from different sequences are plotted in figure 17, where the x-axis is $Z^{0.5}_{\mathrm{EC/PC}}$ and the y-axis is measured $V_{T.50\%}$ (both normalized to data RMS), each dot is one synthesized sequence, and the solid line is fitted to minimize the RMS deviation. The best fitting is $V_{T.50\%} = 0.987\ Z^{0.5}_{\mathrm{EC/PC}} - 0.080$, which astonishingly matches the predicted one $V_{T.50\%} \approx Z^{0.5}_{\mathrm{EC/PC}}$.

To allow a quantitative evaluation of the prediction statistics (given a threshold, we predict the numbers of correct detections and false detections) and its comparison with the benchmarks (given a threshold, we count the number of correct detections and false detections using 'ground truth' data), we have built ROC-typed detection curves as shown in figure 18. The procedures to predict detection statistics have been described as a step-by-step algorithm recipe in section 3.4, where the output is a 'spiking probability map' that tells the chance of the presence of a spike at a given time slot. Given a threshold, the predicted 'spiking probability map' can output detected spike patterns, which have been further compared with the 'ground truth' data to get quantitative feedbacks of positive detections/false detections. If the proposed theory works, ROC curves derived from the 'spiking probability map' should be consistent with ROC curves derived from other detection methods, especially the amplitude-based approach as detections from an analytic signal and from an original signal are more or less equivalent. To be more objective on building the benchmark ROCs, we have tried three types of detection methods: amplitude, nonlinear energy operator and matched filter. As shown in figure 18, the ROC curves derived from predicted 'spiking probability maps' (labeled as EC–PC) are indeed the consistent

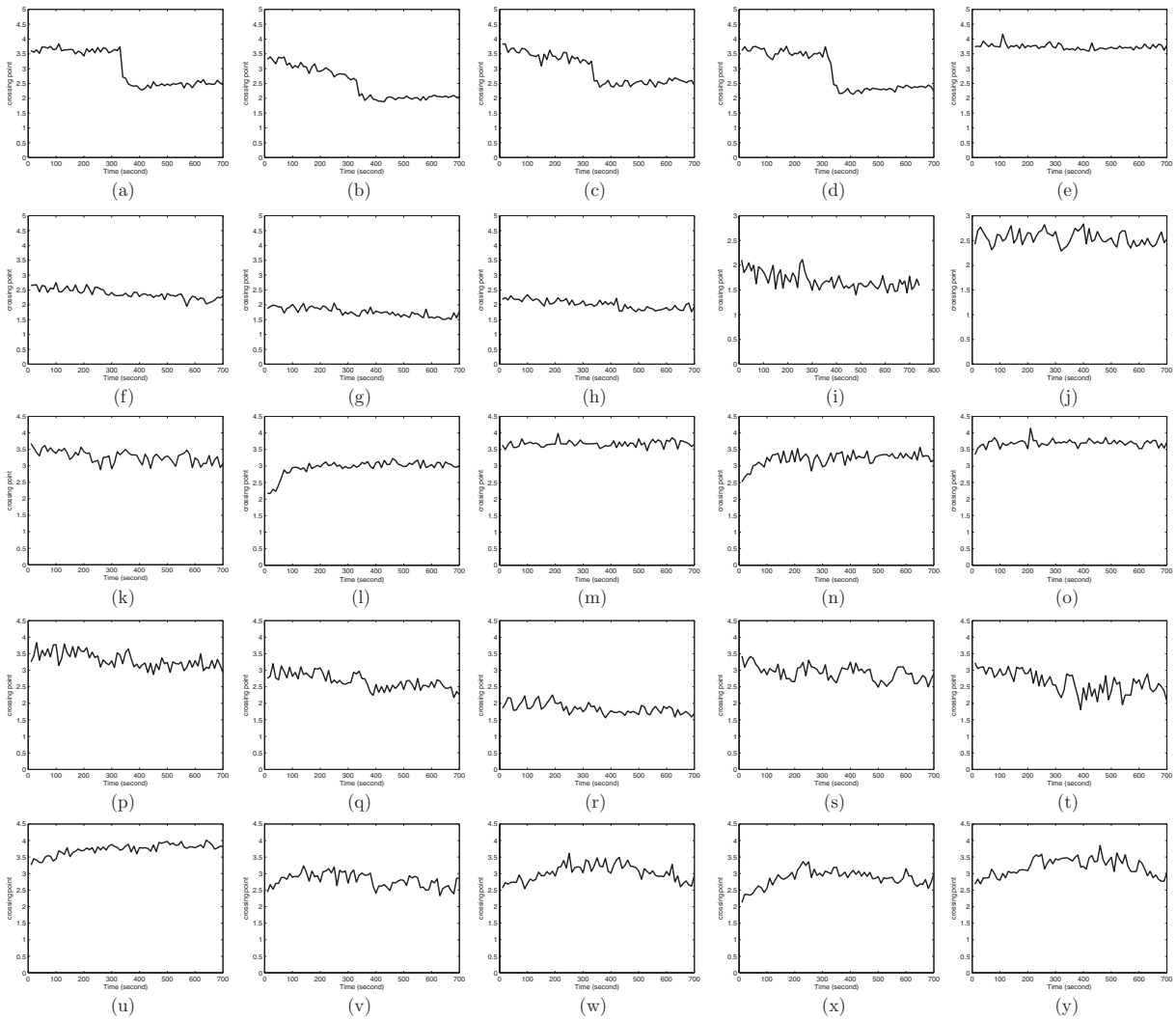

Figure 15. $Z^{0.5}_{EC/PC}$ in multi-channel recording experiment. Each row of figures gives results derived from different channels of one preparation. Five rows are derived from five preparations.

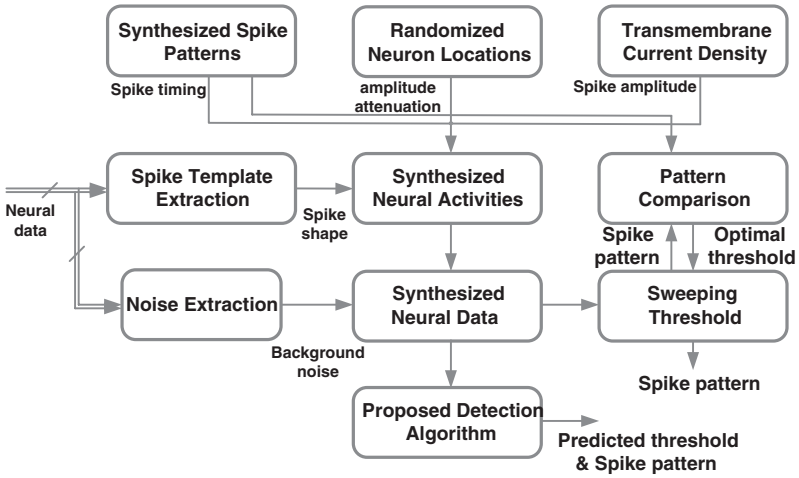

Figure 16. Protocols to synthesize neural data. Neuron noise and a large number of spike templates (spikes over 200 μV) are first extracted from *in vivo* recordings. Background neurons are randomly added around the recording electrode. Each neuron produce spikes from a given template following a randomized inhomogeneous Poisson process. The amplitude of a spike is re-scaled according to the distance between the neuron and the recording electrode with added variation to mimic ion-channel density fluctuations.

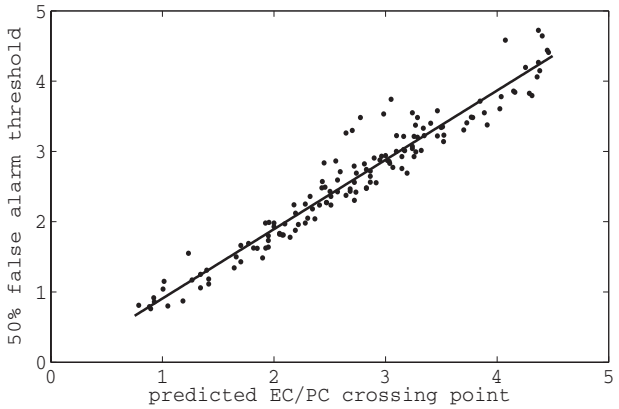

Figure 17. Predicted EC/PC crossing point (x-axis) versus measured threshold (y-axis) that incurs 50% correct detections and 50% false detections ($V_{T.50\%}$). Synthesized sequences are filtered at 300 Hz–5 kHz; Each dot represents one sequence. Neurons are randomly added within a few hundred μm radius of a point electrode. The induced spike amplitude are in a wide range from 5 μV to 1.3 mV; while the RMS noise is 20–30 μV. Best fitting: $y = 0.987x - 0.080$ ($R^2 = 0.935$) compared with the prediction by equations (5), (9) and (10): $y = x$.

benchmarks (labeled as Abs, NEO, MF-Abs) at different SNRs, i.e. 1.5 dB and above, which indirectly validates the spiking probability map.

Figure 19 shows the predicted spiking probability (given data segments of a few ms, the predicted probability that it contains a spike by equation (11)) and its comparison with the measured spiking probability. In this experiment, data segments that have similar predicted spiking probability ($\pm$2.5%) are grouped together and compared with the 'ground truth' data to measure the actual spiking probability. The experiment has shown that the predicted spiking probability is consistent with the measured probability over a wide range of SNRs and firing rates. Results in figures 18 and 19 together confirm that 'spiking probability maps' can be used as *a priori* to estimate an appropriate detection threshold.

5. Summary

A novel theory for modeling *in vivo* neural signals and noise has been presented with rigid experimental verifications. Our study have exposed two statistical components embedded in neural data and shown that they can be used for spike detection. When tested with *in vivo* data, the derived

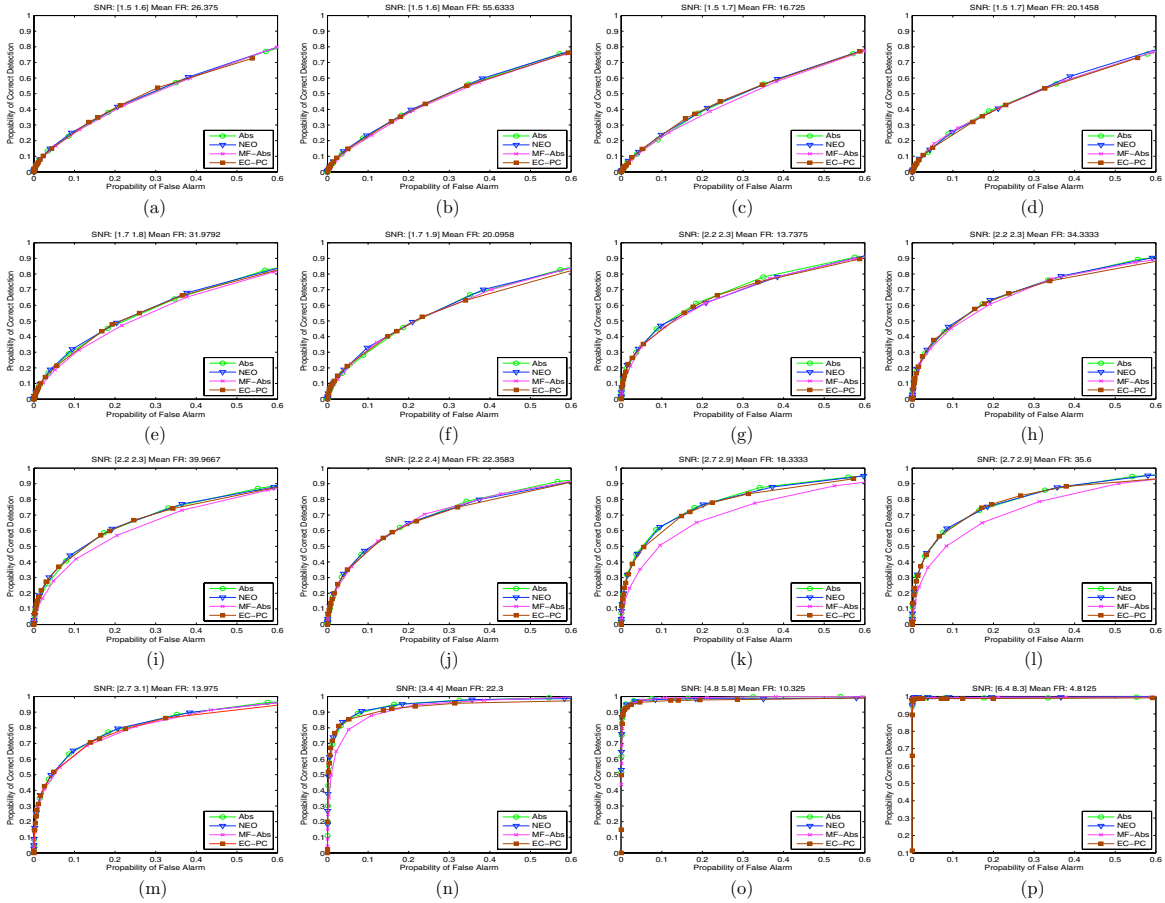

Figure 18. Predicted detection statistics compared with benchmarks. Data are synthesized according to the protocols described in figure 16. The added neurons are grouped according to the SNR (defined as spike amplitude divided by neuron noise RMS), from 1.5 dB SNR in (a) to 8.3 dB in (p) in an increasing order. The x-axis is the probability of false alarm (a detected spike is actually noise); the y-axis is the probability of the correct detections (a detected spike is an added spike). Benchmarks derived from three algorithms, i.e. waveform amplitude (circled green trace, Abs), nonlinear energy operator [18] (triangled blue trace, NEO) and matched filter (crossed magenta trace, MF-Abs) are plotted in comparison with the predicted statistics (squared brown trace, EC–PC) using the derived spiking map (figure 10) by equations (10) and (11).

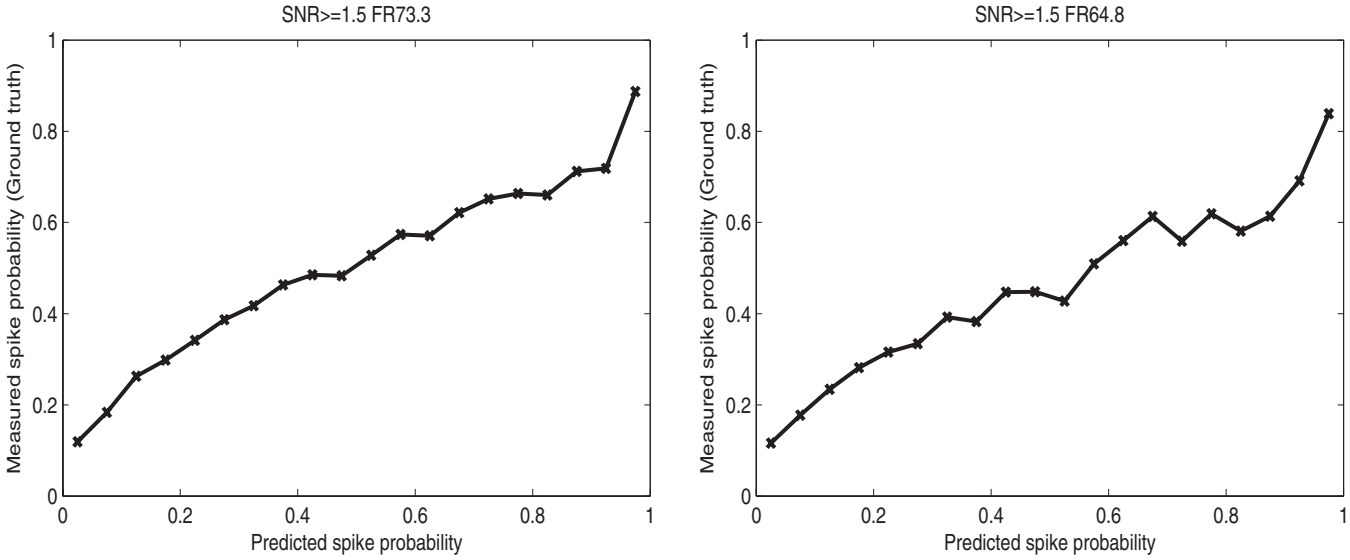

Figure 19. Spiking probability prediction and verification. The *x*-axis is the predicted spiking probability: given a data segment of a few ms, the predicted probability of the presence of a spike; the *y*-axis is the measured spiking probability: data segments that have similar predicted spiking probabilities (±2.5%) are grouped together and compared with the 'ground truth' data to measure the actual spiking probability. (a) 40 neurons with an averaged firing rate of 1.8 Hz and (b) 30 neurons with an averaged firing rate of 2.1 Hz are included. The data preparation protocol follows figure 16. The summed spiking rate in the experiment is set to below 100 Hz to avoid bias to detection.

threshold exhibits significant variations from 23 to 155 μV (1–6 RMS), suggesting that the conventional approach of fixing the threshold at a constant rms level is not reliable and may cause significant losses in information. In addition, $Z^{0.5}_{\mathrm{EC/PC}}$ (the threshold corresponds to 50% positive detection and 50% false alarm) may change over time and vary from one channel to a different channel, which requires the training algorithms to be independent over different channels and adaptive over time. When tested with synthesized data, the predicted ROC curves match the benchmarks at a varied SNR and the predicted spiking probability is consistent with the measurement. We envision that this work may be applied to a wide range of experiments as a front-end data analysis tool.

6. Protocol

Rat data are provided by Dr Edward Keefer at Plexon Inc. The protocols can be found in [46]. Cat data are provided by Dr Victor Pikov at Huntington Medical Research Institute. The neural recordings were collected from the cerebral cortex in several cats, as previously described [47]. Briefly, the 16-channel (4 × 4) electrode arrays with a nominal geometric area of exposed electrode tips of 2000 μm^2 were purchased from Blackrock Microsystems. To decrease the electrode impedance, the electrodes were coated with the sputtered iridium oxide (SIROF) at the EIC Labs using the previously established procedure [48]. The array was chronically implanted in the sensorimotor cortex and connected to a percutaneous connector mounted in the animal's head, in accordance with the HMRI Institutional Animal Care and Use Committee-approved protocol and in compliance with the USDA Animal Welfare Act. At 10–100 days after the array implantation, the animal was lightly anesthetized by an intramuscular injection of ketamine (11 mg kg^{-1}) and acepromazine (0.1 mg kg^{-1}), allowing the animal to breathe on its own and to limit the suppression of spontaneous cortical neuronal activity. Neural data were recorded at 16 bit and 25 ksps using a custom amplifier and a data acquisition board (USB-6259, National Instruments).

Acknowledgments

The authors acknowledge Dr Edward Keefer at Plexon for providing part of the experiment data and Harvey Wiggins at Plexon for helpful suggestions. This research was supported by National University of Singapore grant (R-263-000-619-133), A∗STAR PSF grant (R-263-000-699-305) and A∗STAR SERC grant (R-263-000-656-305).

References

[1] Koch C 2004 *The Quest for Consciousness: A Neurobiological Approach* (Greenwood Village, CO: Roberts)
[2] Scherberger H, Jarvis M and Andersen R 2002 Cortical local field potential encodes movement intentions in the posterior parietal cortex *Neuron* **46** 347–54
[3] Buzsaki G 2006 *Rhythms of the Brain* (Oxford: Oxford University Press)
[4] Balduzzi D and Tononi G 2009 Qualia: the geometry of integrated information *PLoS Comput. Biol.* **5** 1–24
[5] Hausser M, Spruston N and Stuart G 2000 Diversity and dynamics of dendritic signaling *Science* **290** 739–44
[6] Quiroga R, Reddy L, Kreiman G and Koch C 2005 Invariant visual representation by single neurons in the human brain *Nature* **435** 1102–7
[7] Sheffield M, Best T, Mensh B, Kath W and Spruston N 2011 Slow integration leads to persistent action potential firing in distal axons of coupled interneurons *Nature Neurosci.* **14** 200–7

[8] Brown E, Kass R and Mitra P 2004 Using multi-neuron population recordings for neural prosthetics *Nature Neurosci.* **7** 456–61

[9] Hochberg L *et al* 2006 Neuronal ensemble control of prosthetic devices by a human with tetraplegia *Nature* **442** 164–71

[10] Maass W, Natschlager T and Markram H 2002 Real-time computing without stable states: a new framework for neural computation based on perturbations *Neural Comput.* **14** 2531–60

[11] Cunningham J, Yu B, Shenoy K and Sahani M 2008 Inferring neural firing rates from spike trains using Gaussian processes *Adv. Neural Inf. Proc. Syst.* **20** 329–36

[12] Gerstner W, Kreiter A, Markram H and Herz A 1997 Neural codes: firing rates and beyond *Proc. Natl Acad. Sci.* **94** 12740

[13] Stein R, Gossen E and Jones K 2010 Neuronal variability: noise or part of the signal? *Nature Rev. Neurosci.* **6** 389–97

[14] Kumar A, Rotter S and Aertsen A 2010 Spiking activity propagation in neuronal networks: reconciling different perspectives on neural coding *Nature Rev. Neurosci.* **11** 615–27

[15] Stevenson I and Kording K 2011 How advances in neural recording affect data analysis *Nature Neurosci.* **14** 139–42

[16] Dolan K, Martens H C F, Schuurman P R and Bourm L J 2009 Automatic noise-level detection for extra-cellular micro-electrode recordings *Med. Biol. Eng.* **47** 791–800

[17] Lewicki M S 1998 A review of methods for spike sorting: the detection and classification of neural action potentials *Netw. Comput. Neural Syst.* **9** 53–78

[18] Mukhopadhyay S and Ray G C 1998 A new interpretation of nonlinear energy operator and its efficacy in spike detection *IEEE Trans. Biomed. Eng.* **45** 180–7

[19] Kim K and Kim S J 2003 A wavelet-based method for action potential detection from extracellular neural signal recording with low signal-to-noise ratio *IEEE Trans. Biomed. Eng.* **50** 999–1001

[20] Obeid I and Wolf P D 2004 Evaluation of spike-detection algorithms fora brain–machine interface application *IEEE Trans. Biomed. Eng.* **51** 951–11

[21] Buzsaki G 2004 Large-scale recording of neuronal ensembles *Nature Neurosci.* **74** 46–451

[22] Scherberger H, Jarvis M R and Andersen R A 2005 Spike detection using the continuous wavelet transform *IEEE Trans. Biomed. Eng.* **52** 74–87

[23] Rutishauser U, Schuman E M and Mamelak A N 2006 Online detection and sorting of extracellularly recorded action potentials in human medial temporal lobe recordings, *in vivo J. Neurosci. Methods* **154** 204–24

[24] Rizk M, Obeid I, Callender S and Wolf P 2007 A single-chip signal processing and telemetry engine for an implantable 96-channel neural data acquisition system *J. Neural Eng.* **4** 309–21

[25] Shahid S, Walker J and Smith L S 2010 A new spike detection algorithm for extracellular neural recordings *IEEE Trans. Biomed. Eng.* **57** 853–66

[26] Franke F, Natora M, Boucsein C, Munk M and Obermayer K 2010 An online spike detection and spike classification algorithm capable of instantaneous resolution of overlapping spikes *J. Comput. Neurosci.* **29** 127–48

[27] Gibson S, Judy J W and Markovic D 2010 Technology-aware algorithm design for neural spike detection, feature extraction, and dimensionality reduction *IEEE Trans. Neural. Syst. Rehabil. Eng.* **18** 467–78

[28] Salmanpour A, Olson B and Si J N 2010 Spike detection in human muscle sympathetic nerve activity using a matched wavelet approach *J. Neurosci. Methods* **193** 343–55

[29] Yang C H, Olson B and Si J N A 2011 Multiscale correlation of wavelet coefficients approach to spike detection *Neural. Comput.* **23** 215–50

[30] Maragos P, Kaiser J F and Quatieri T F 1993 On amplitude and frequency demodulation using energy operators *IEEE Trans. Signal Process.* **41** 1532–50

[31] Teich M, Johnson D, Kumar A and Turcott R 1990 Rate fluctuations and fractional power-law noise recorded from cells in the lower auditory pathway of the cat *Hear. Res.* **46** 41–52

[32] Davidsen J and Schuster H Z 2002 Simple model for $1/f^{\alpha}$ noise *Phys. Rev. Lett.* **65** 026120

[33] Yu Y, Romero R and Lee T S 2005 Preference of sensory neural coding for 1/f signals *Phys. Rev. Lett.* **94** 108103

[34] Bedard C, Kroger H and Destexhe A 2006 Does the $1/f$ frequency scaling of brain reflect self-organized critical states? *Phys. Rev. Lett.* **97** 118102

[35] Hassibi A, Navid R, Dutton R W and Lee T 2004 Comprehensive study of noise processes in electrode electrolyte interfaces *J. Appl. Phys.* **96** 1074–82

[36] Razavi B 2001 *Design of Analog CMOS Integrated Circuits* (Boston, MA: McGraw-Hill)

[37] Yang Z, Zhao Q, Keefer E and Liu W 2009 Noise characterization, modeling, and reduction for *in vivo* neural recording *Adv. Neural Inf. Process. Syst.* **22** 2160–8

[38] Rice J 1995 *Mathematical Statistics and Data Analysis* (Belmont, CA: Duxbury)

[39] Billingsley P 1995 *Probability and Measure* (New York: Wiley)

[40] Klartag B 2007 A central limit theorem for convex sets *Invent. Math.* **168** 91–131

[41] Davidson J 1992 A central limit theorem for globally nonstationary near-epoch dependent functions of mixing processes *Econometr. Theory* **8** 313–29

[42] Gabor D 1946 Theory of communication *J. Inst. Electr. Eng.* **93** 429–57

[43] Schafer C, Rosenblum M G, Abel H H and Kurths J 1999 Synchronization in the human cardiorespiratory system *Phys. Rev.* E **60** 857–70

[44] King F 2009 *Hilbert Transforms* (Cambridge: Cambridge University Press)

[45] Steel R and Torrie J 1960 *Principles and Procedures of Statistics* (New York: McGraw-Hill)

[46] Keefer E W, Botterman B R, Romero M I, Rossi A F and Gross G W 2008 Carbon nanotube-coated electrodes improve brain readouts *Nature Nanotech.* **3** 434–9

[47] Kane S R, Cogan S F, Ehrlich J, Plante T D and McCreery D B 2011 Electrical performance of penetrating microelectrodes chronically implanted in cat cortex *Proc. 33th Annu. Int. Conf. IEEE EMBS* pp 5416–9

[48] Cogan S F *et al* 2009 Sputtered iridium oxide films for neural stimulation electrodes *J. Biomed. Mater. Res.* B **89** 353–61